J. Eur. Opt. Society-Rapid Publ. 2025, **21**, 7
© The Author(s), published by EDP Sciences, 2025
https://doi.org/10.1051/jeos/2025002
Available online at: https://jeos.edpsciences.org

Journal of the European Optical Society-Rapid Publications

EOSAM 2024
Guest editors: Luca De Stefano and Raffaele Velotta

RESEARCH ARTICLE OPEN ACCESS

Resolution enhancement methods in optical microscopy for dimensional optical metrology

Mohammad Nouri[1,2], Paolo Olivero[3], Stefanie Kroker[1,2], Tim Käseberg[2], Ivano Ruo-Berchera[4], Bernd Bodermann[2,*], Himanshu Tyagi[5], Deb Roy[5], Deshabrato Mukherjee[6], Thomas Siefke[7], Poul Erik Hansen[8], Astrid Tranum Rømer[8], Miroslav Valtr[9], Pietro Aprà[10], and Peter Petrik[6,11]

[1] Institut für Halbleitertechnik, Laboratory for Emerging Nanometrology, Technische Universität Braunschweig, Hans-Sommer-Str. 66, 38106 Braunschweig, Germany
[2] Physikalisch-Technische Bundesanstalt, Bundesallee 100, 38116 Braunschweig, Germany
[3] Physics Department, University of Torino, via P. Giuria 1, 10125 Torino, Italy
[4] Istituto Nazionale di Ricerca Metrologica, Strada delle Cacce 91, 10135 Torino, Italy
[5] Swansea University, Singleton Park, Swansea SA28PP, Wales, UK
[6] Institute of Technical Physics and Materials Science, Konkoly Thege Str. 29-33, Budapest, 1121, Hungary
[7] Institute of Applied Physics, Abbe Center of Photonics, Friedrich Schiller University Jena, Albert-Einstein-Strasse 15, Jena, 07745, Germany
[8] DFM, Danish National Metrology Institute, Kogle Allé 5, 2970 Hørsholm, Denmark
[9] Czech Metrology Institute, Okružní 31, 638 00 Brno, Czech Republic
[10] National Institute of Nuclear Physics (INFN), Torino Section, via Pietro Giuria, 10125 Torino, Italy
[11] Department of Electrical Engineering, Institute of Physics, Faculty of Science and Technology, University of Debrecen, Bem ter 18, Debrecen, 4026, Hungary

Received 30 August 2024 / Accepted 7 January 2025

Abstract. In this paper, we discuss several enhancement approaches to increase the resolution and sensitivity of optical microscopy as a tool for dimensional nanometrology. Firstly, we discuss a newly developed through-focus microscopy technique providing additional phase information from the afocal images to increase the nanoscale sensitivity of classical microscopy. We also explore different routes to label-free or semiconductor compatible labelling super-resolution microscopy suitable for a broad range of technical applications. We present initial results from, a new wide-field super-resolution imaging technique enabled by Raman scattering. In addition, we discuss super-resolution imaging using NV centres in nano-diamonds as labels and their application in future reference standards.

Keywords: Nitrogen-vacancy (NV) centres, STED microscopy, Photoluminescence, Label-free super-resolution, Optical nanometrology, Through-focus microscopy, Non-linear Raman super-resolution.

1 Introduction: A path to universal imaging nanometrology

Complex micro- and nano-scale structures of different materials are the basis of the development and fabrication of modern and future electronic and optical devices. Typically, the functionalities of these devices crucially depend on the size e.g. the line width or critical dimension and other shape details of the structures. Therefore, accurate, reliable, and efficient dimensional metrology is mandatory both for development and manufacturing process and quality control. Although sophisticated nanoscale metrology methods based on charged particles (such as scanning electron microscopy SEM, transmission electron microscopy TEM, Helium ion microscopy HIM or scanning tunnelling microscopy STM), X-Rays (transmission (TSAX) or grazing incidence (GISAX) small angle X-ray scattering) or tactile probes (e.g. Atomic Force Microscopy AFM) are available (cf. for example [1] and references therein), optical methods such as optical microscopy and scatterometry are advantageous due to their non-destructive nature, high speed and good in-line capability [2].

Achieving reliable and precise measurements for analysing these structures is a challenge for various fields of science and industry. Non-imaging optical methods like scatterometry or ellipsometry, in semiconductor metrology

* Corresponding author: bernd.bodermann@ptb.de

This is an Open Access article distributed under the terms of the Creative Commons Attribution License (https://creativecommons.org/licenses/by/4.0), which permits unrestricted use, distribution, and reproduction in any medium, provided the original work is properly cited.

denoted as optical critical dimension (OCD) metrology, have proven astonishing capabilities in dimensional nanometrology down to the few-Nanometre feature size regime. However, they are limited to periodic structures, require relatively large target fields and provide only mean integral measurement values for structure parameters [3, 4]. For several applications like field effect transistors (FET), local defect characterisation or to characterise local parameter variations, imaging metrology is indispensable ([1, 2], and references therein).

Optical microscopy is a metrology technique to provide physical information about samples with sufficient contrast. It is the method of choice for spatial measurements of individual structures. However, conventional optical microscopy suffers from a fundamental resolution limit due to diffraction [5]. Therefore, several methods have been developed and applied to increase the sensitivity to specific structural features and the measurement capabilities of optical microscopy for nanoscale structures and features: Different types of interference microscopy is adding phase information to the microscope image, which can enhance the sensitivity and signal-to-noise ratio to specific nanoscale features [6]. Phase information without the need of reference fields can also be obtained by detection of different afocal images in Through Focus Microscopy (TFM). Besides phase information, Tomographic Diffractive Microscopy (TDM) is adding additional spatial frequency information by artificial aperture extension. This is achieved by the application of different combinations of illumination and detection schemes, which can provide even higher contrast and resolution images [7]. However, TFM and, to a significantly larger degree, TDM require numerical calculations to provide (purely computational) high quality images of the nanostructures under test. Another interesting approach is Alternating Grazing Incidence Darkfield Microscopy (AGID), which can extend the measurement capability of the widths of individual structures down to 1/10 of the wavelength used [8, 9].

Microscopy methods such as scatterfield microscopy [10] or through-focus microscopy [11] have been developed and tested for quantitative dimensional metrology on (deep) sub-wavelength structures. These do not belong to the classical super resolution techniques but show astonishing sensitivity regarding sub-resolution features, allowing for CD measurements down to a few 10 nm.

In Section 2, we present a through-focus microscopy method and a corresponding metrology system developed at the Danish National Metrology Institute (DFM), which can be seen as a sophisticated reference system of what can be achieved with "classical" (i.e. non-super-resolution) microscopic measurement systems.

In recent decades, many super-resolution microscopy (SRM) techniques that exceed the lateral and/or axial resolution limit have been developed [12, 13]. Focusing on far-field methods, SRM methods can roughly be classified in four different approaches:

1. Far-field techniques derived from objective modifications or metamaterial based super-lenses which in principle can detect high spatial frequency information from label-free samples [13].
2. Non-uniform illumination/collection, including linear and non-linear structured illumination microscopy (SIM) [14–17].
3. Deterministic functional pump/probe techniques such as stimulated emission depletion (STED) microscopy [18, 19] based on switch-able detection channels (mainly via molecular state population modifications) and non-linear interactions.
4. Stochastic functional opto-numerical SRM methods such as photo-activated localization microscopy (PALM) [20] or stochastic optical reconstruction microscopy (STORM) [21].

Many of these methods offer an excellent optical resolution down to a few nm. However, while the objective modification or super-lens methods are often very limited in practical applications and in some cases convincing experiment verifications are missing the other SRM methods are mostly based on fluorescence microscopy. They typically require specific sample preparations with fluorescence markers (labels) and are therefore mainly suitable for biological samples, but usually not accessible for inorganic applications such as semiconductor metrology.

In recent years, in fact also many very interesting approaches have been discussed and partly also demonstrated experimentally to provide label-free SRM. An excellent overview is given by Astratov [13]. However, most of this research has focussed on qualitative imaging, often still on biological samples, and fluorescence microscopy and many methods are limited to very specific applications or materials.

What still is missing for applications in quantitative nanoscale optical metrology is a universal label-free SRM suitable for (dimensional) nanometrology in technical applications and inorganic materials, which has the potential to complement for example OCD metrology in semiconductor manufacturing.

Therefore, in the context of a larger European research project (European Metrology Programme for Innovation and Research) [22], several partners have been cooperating to investigate potential options and develop promising methods to reach this goal [23]. This article is giving an overview about different methods which have been investigated and developed within our consortium to achieve such label free SRM options or at least SRM methods with alternative labelling schemes acceptable and suitable for dimensional metrology and technical applications.

Different routes and approaches for label-free or alternative-label SRM (Sect. 3) have been analysed theoretically.

In Section 4, two promising methods are described in more detail and with first experimental results: Wide-field Imaging with Super-resolution Enabled signal (WISER, Sect. 4.2) and a STED-like pump-probe method for NV centres in artificial diamond as an example for STED microscopy of inorganic materials with suitable four-level systems (Sect. 4.3).

In Section 5 we shortly discuss which, either from our research or beyond, are from our perspective the most promising routes to a universal microscopic-optical

nanometrology free of unwanted fluorescence labelling. Finally, we end with a short conclusion and outlook (Sect. 6).

2 Enhancement of classical light microscopy by through-focus microscopy

In microscopy, a typical task is to determine the distance between two points on a surface. From this spatial resolution is defined as the ability to distinguish two points like objects on from a single object. Vertical resolution is not uniquely defined in microscopy. Most often we speak about the ability to distinguish two separated neighbouring point like objects on a surface at different vertical positions from a single object. However, in microscopy we can create a 3D image of the object by making a vertical image stack of 2D images. The separation between the 2D images is related to axial resolution of the microscope, which is the ability to separate two points like objects on the axial line from a single object.

Classical bright-field optical microscopy is the simplest, most widely used system for dimensional metrology at the micro- to nanoscale. However, due to diffraction the spatial resolution is limited to about $\lambda/(2\mathrm{NA})$ according to the Rayleigh limit, where NA is the numerical aperture [24]. The axial resolution is limited by the depth of field of the microscope, which may be estimated by $2\lambda/(\mathrm{NA}^2)$.

Scanning confocal microscopy offers several advantages over bright-field microscopy, including the ability to control depth of field and reducing the scattered light away from the focal plane, the capability to serial image thick objects, and the ability to achieve high lateral resolution. The key to confocal advantages is the use of spatial filtering with a pinhole to eliminate out-of-focus light from the object and the use of a laser or narrow line-width LED to form a coherent imaging system. A coherent imaging system is described by linear addition of the fields from the object, whereas a normal incoherent bright-field microscope is described by linear addition of intensities. The point-spread function (PSF) is a measure of the resolving power of a microscope and the observed microscope image is the convolution between the true image and the PSF. The true image may in principle be obtained by deconvolving the observed picture with the PSF of the microscope, if the PSF is known. However, in reality we only get an improved image due to the lack of available information. The deconvoluted image is the limit of classical light microscopy with a typical spatial resolution limit of approximately 75 nm for scanning confocal microscopy working in the visible wavelength range [25].

Through-focus confocal microscopy (TFCM) is a technique, in which the image is obtained using inverse methods, where a simulated image stack is compared to the measured image stack to obtain the best fit [25, 26]. The phase information in the complex fields usually requires rigorous treatment of the light-matter interaction and the light propagating through the microscope. The first step for a partially resolved image is to improve the measured image by deconvolution with the PSF of the microscope. This image is used to extract the starting values for the inverse modelling.

Here we present a digital twin of an optical microscope focusing on TFCM. The working principle of the digital twin can be described by the following steps:

1. The incident field is a normal incident wave with a normalized k-vector $(0, 0, 1)^{\mathrm{T}}$ in the back focal plane.
2. The light beam coordinate system defined by the unit vectors for TE-amplitude, TM-amplitude, and k-vector is used to describe the optical propagation.
3. The response from the periodic structure is calculated as a Jones matrix using the Fourier modal method.
4. All the points that enter the same pixel in the back focal plane are added coherently. The 2D image formation is done by focusing the far-field angular scattering in the back focal plane for a given vertical position onto the image plane.
5. The 3D image is obtained by performing 2D image formations for all vertical (z) positions and stacking the 2D images (see Fig. 1).
6. For confocal microscopy imaging the 3D image is a set of data points (x, y, z) from the 2D image stack. For each lateral position (x, y), the z value is obtained as the z position in the 2D image stack, for which the intensity is maximal.

We have performed TFCM simulations of silicon line gratings with a pitch of 250 nm, 300 nm and 400 nm of ridge height 138 nm (for the smallest pitches) and a ridge height of 148 nm for the largest pitch. In the simulations, we use light of wavelength 405 nm and an objective with NA = 0.95. We demonstrate that TFCM simulations resolve these lateral pitch structures and that the resolution along the z direction is improved by deconvolution of the PSF of the objective.

We obtain the PSF by Fourier transformation of the optical transfer function, which is defined by a step function in cylindrical coordinates [27]. The components of the light propagation vector in the lateral directions (k_x, k_y) are defined by $\sqrt{{k_x}^2 + {k_y}^2} \leq \frac{2\pi}{\lambda} \cdot \mathrm{NA}$. The out-of-plane propagation vector is defined by $k_z = \sqrt{(2\pi/\lambda)^2 - {k_x}^2 - {k_y}^2}$ which enters the out-of-focus phase factor of the PSF given by $e^{ik_z z}$. The image step size defines the sampling in spatial-frequency space. Figure 2 shows the result of applying this procedure to the silicon line grating with pitch of 300 nm.

In a real microscope measurement, the procedure is slightly different. First, the sample is measured, and we observe the measured profile given by the black line in Figure 2. Secondly, we do a deconvolution to improve the optical profile to find a good starting point for TFCM inverse modelling. Thirdly, we calculate simulated optical profiles from simulated z-stack images to find the simulated optical profile that best match the measured optical profile (black curve). The shape of the measured optical profile is found from knowledge of the shape for the best matching simulated profile.

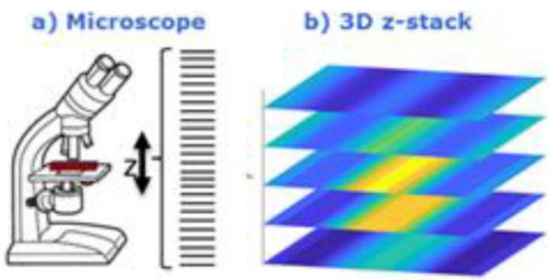

Figure 1. (a) Vertical scanning of a microscope. One image is taken at each vertical position. (b) 3D image stack for CM and TFCM.

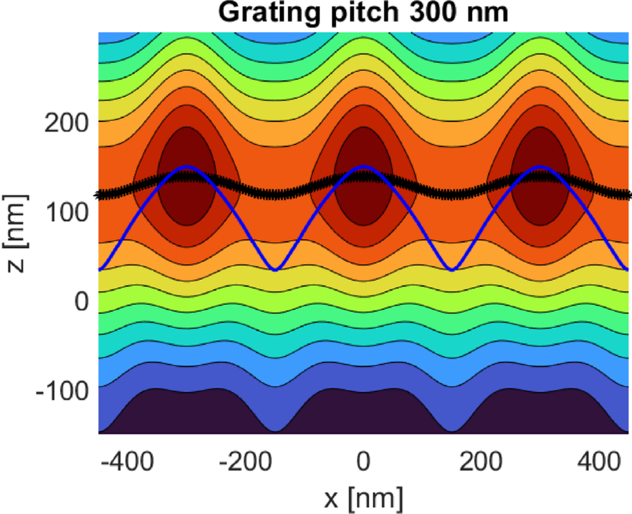

Figure 2. Height of grating profile obtained from z-stack image profile (multi colours), grating profile (black stars) from z-stack image directly and grating profile after (blue line) deconvolution of the z-image stack. The nominal height is 138 nm, and the pitch is 300 nm. The intensity of the z-image stack is shown by the colour scale in the background.

3 Label-free super-resolution microscopy for dimensional metrology

As indicated in Section 1, the main goal of our research is to investigate and develop universal methods of imaging optical nanometrology based on label-free SRM techniques. The intended applications in (dimensional) nanometrology define some specific requirements:

1. Universality: the method should allows to cover a broad range of applications, both in terms of materials (particularly including inorganic) and structures to be characterised to enable dimensional nanometrology for important applications such as semiconductor, nanophotonics or other nanotechnologies.
2. Label-free or "acceptable labelling": A conditioning with organic molecules as fluorescence markers is typically not acceptable e.g. for wafer manufacturers, so that in the best case a label-free metrology method would be required. However, a thin layer with an alternative, preferable inorganic and stable markers e.g. on top or within the substrate could be acceptable as well, as long as the intended device manufacturing and function is not affected.
3. Ease of use: The metrology methods should not be too complex and time-consuming both on the measurement and on the data analysis side in order to enable in-line measurements in particular.
4. Potential for quantitative measurement and traceability: The difference between imaging and imaging metrology is the reliable and traceable quantification. This requires a stable deterministic measurement process with a good reproducibility and a good understanding and control of the whole measurement process. Since today nearly any sophisticated metrology requires a reliable and efficient modelling of the whole measurement process, it is required to have a good understanding and efficient means to model particularly the light-structure interaction, e.g. with the help of Maxwell solvers. Traceability of the measurement means that any measurement parameter (such as the microscope magnification or sample movement) must be traced back to the corresponding SI units. This can be supported or achieved e.g. by access to suitable calibrated reference standards [28].

Requirement 4 is the reason why in our research we did not consider stochastic functional opto-numerical SRM methods such as STORM, since besides the difficulties in finding stochastic labels alternative to fluorescence markers the stochastic nature of the imaging process would make it, at least, a big challenge to provide traceability.

In the following, we will shortly discuss a number of different label-free SRM methods and consider their potential for dimensional metrology. Many of them have already been extensively described and summarised in [13], and some have been developed or improved within our research.

Regarding the classification given in Section 1, most approaches to achieve label-free SRM are either based on non-uniform illumination/collection (SIM and related methods), or deterministic functional pump/probe techniques following the basic principles of STED or, more generally, RESOLFT [29] (reversible saturable optical linear (fluorescence) transition) microscopy methods.

3.1 Methods based on non-uniform (structured) illumination

If we consider an optical imaging system with an imaging numerical aperture $\mathrm{NA}_{\mathrm{Img}}$, then $k_0 = 2\mathrm{NA}_{\mathrm{Img}}/\lambda_{\mathrm{em}}$ (λ_{em} being the wavelength of the light used for imaging) is the modulus of the wavevector corresponding to the cut-off frequency $\omega_0 = c \cdot k_0$ the spatial frequency which can be transmitted by the optical imaging system. SIM is a non-uniform illumination/collection method that extends resolution through the extraction of higher spatial frequency information beyond this cut-off wavevector k_0, and transferring it into an observable region of conventional microscopy in the form of Moiré fringes [15]. It can be considered as a

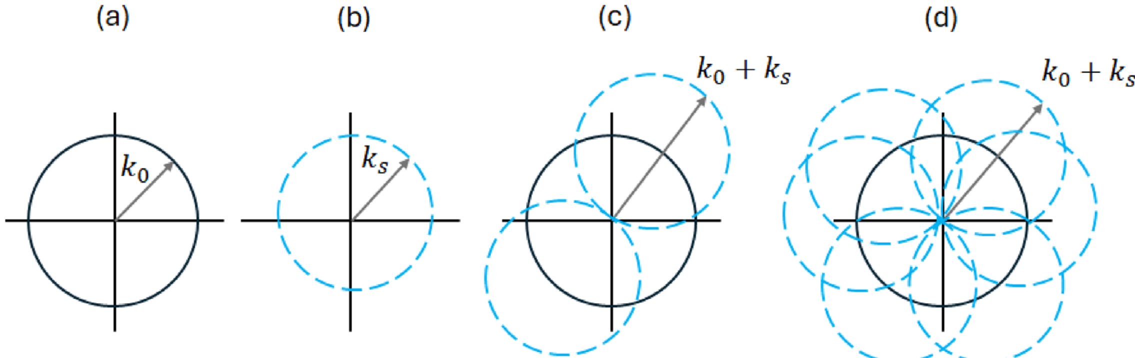

Figure 3. Schematic of the mechanism of expanding the Fourier frequency of collecting the spatial distribution of the signals for imaging. (a) Wave vector in the Fourier space of signal collection using an objective lens from a diffraction limited spot, (b) Fourier space augmented by the projected structured line with wave vector (k_s), (c) combined wave vector of the objective and the structured light in one direction, and (d) The combined Fourier space addressed using the microscope.

heterodyne detection of spatial frequencies ω_{object} of the object under test. The structured illumination provides a local oscillator spatial frequency $c \cdot k_s$ and it is shifting (or folding) spatial frequency components of the object image within the range of $\omega_s - \omega_0$ and $\omega_s + \omega_0$ (Fig. 3).

3.1.1 Linear SIM

SIM has been introduced by Gustafsson [15] and has shown to provide images of fluorescent objects with an up to two-fold resolution enhancement compared to wide-field microscopy. The reason for this limitation is because the structured illumination used is typically provided by an interference pattern, which is illuminating the object via the illumination optics of the microscope. Therefore, the local oscillator frequency is limited by the bandwidth of the illumination optics $\omega_{0,\text{ ill.}}$ which usually is smaller or equal to the bandwidth of the imaging optics:

$$\omega_s \leq \omega_{0,ill.} \leq \omega_0.$$

SIM can be easily applied also for non-fluorescent objects, i.e. it can be adapted for label-free SRM as well. The structured illumination can also be achieved by spatio-temporal fast scanning of a small light spot, e.g. a focussed laser beam [30]. In principle, this opens the option to achieve higher local oscillator frequencies $\omega_s > \omega_0$ if a sub-diffraction light spot can be created and quickly scanned over the object. In this direction recently we investigated options to create such small controllable light spot e.g. by using novel plasmonic lens concepts [31] or by fast scanning photonic nano-jets [32].

3.1.2 Non-linear SIM

To extend the spatial frequency of the local oscillator, nonlinear interactions such as saturation or multi-photon processes can be used. In saturated structured illumination microscopy (SSIM) [16] the non-linearity results from the saturation of excitation states, which generate higher order of harmonics in the detection (typically fluorescence) signal, which can be used as local oscillators with higher spatial frequencies well above the cut-off frequency $\omega_s >> \omega_0$. The high order harmonics can expand the optical bandwidth, resulting in a better resolution than conventional SIM. Although the SSIM resolution is theoretically unlimited, the signal-to-noise ratio practically limits the resolution. Gustafsson et al showed a resolution in the order of 50 nm on a fluorescence sample using this technique [16, 17].

The SIM technique can be applied for other nonlinear light-matter interactions, such as Raman scattering microscopy, coherent anti-Stokes Raman scattering (CARS) microscopy as well as second harmonic generation (SHG) and third harmonic generation (THG) microscopy. SHG and THG microscopies have emerged as powerful imaging modalities to examine the structural properties of label-free samples [33]. However, the SHG process requires the environment to be non-centrosymmetric at the excitation wavelength scale, whereas the THG process requires a medium with intrinsic inhomogeneities due to a refractive index mismatch [34, 35]. Typical lateral resolution in SHG and THG is limited to the longer excitation wavelength and lower numerical aperture [35]. Therefore, the resolution improvement with these techniques is a challenge. Huttunen et al. [36] proposed a coherent nonlinear SIM scheme based on spatially modulating the phase of the incident field and using interferometric detection for extracting the emitted complex-valued field. With this method, lateral resolution can be improved four- and six-fold for SHG and THG processes, respectively.

In the context of SIM for inelastic scattering such as Raman scattering, the spatial distribution of Raman scatterer is excited with structured excitation light intensity. Since the light emitted from a point is proportional to the product of the amount of Raman scatterer and the local excitation light intensity, a beat pattern, known as Moiré fringes, will appear in the observed image. The spatial resolution obtained in such a configuration is (see Fig. 3):

$$d_s = \frac{1}{(k_0 + k_s)}.$$

Since the highest spatial frequency that can be imposed by the same objective can be k_0, the maximum resolution obtainable in this scheme is:

$$d_{\max} = \frac{1}{2k_0}.$$

This formulation is valid for 1st order linear Raman scattering. However, if the order of the scattering is higher, the maximum k_s becomes proportional to the order of the scattering e.g. $k_s = 2k_0$ for 2nd order non-linearity processes and $k_s = 3k_0$ for 3rd order non-linearity processes leading to spatial resolution of $1/3k_0$ and $1/4k_0$ respectively. Unlike fluorescence signals, Raman signals are significantly narrower. Therefore, the method requires a narrow band filter and a spectrometer to achieve the chemical specificity.

The application of the CARS process to microscopy provides chemical information about a sample without labelling agents. The contrast in CARS microscopy arises from the signal enhancement when the frequency difference between the pump field ω_{pump} and the stokes field ω_{Stokes} is tuned to a Raman-active vibrational band [37, 38]. Unlike fluorescence imaging, CARS measurements are not background free. The non-resonant background from any objects of interest and the surrounding solvent limits the image contrast and spectral selectivity [37]. Several methods and strategies have been suggested for suppressing or separating the non-resonant background, including using a near-IR beam, polarization-resolved CARS, epi-detection CARS, and heterodyne CARS [39–41]. Also, the signal of the CARS process relies on the satisfaction of a phase-matching condition between wave vectors of the excitation and emission fields ($k_{\text{CARS}} = 2 \cdot k_{\text{pump}} - k_{\text{Stokes}}$, where k_{CARS}, k_{pump}, and k_{Stokes} are the CARS signal (anti-Stokes), the pump and the Stokes wave vector, respectively) [42]. Additionally, the lateral resolution of CARS microscopy is diffraction-limited which depends directly on the CARS-signal wavelength λ_{CARS}, and inversely on the numerical aperture of the detection system NA_{det} [43]. Therefore, adding super-resolution capability to CARS microscopy as a label-free super-resolution technique is a challenge.

To address this issue, Park et al. and Hajek et al. proposed a theoretical scheme based on SIM to improve the resolution of CARS microscopy. Park et al. demonstrated that the coherent image formation with the non-linear structured excitation framework has a potential to enhance resolution 2.7 times better than the conventional wide-field CARS system [43]. Hajek et al. theoretically showed that adding the structured illumination to the wide-field CARS configuration as a standing wave for the pump beam can improve the lateral resolution three-fold [44]. In summary, SIM based on the coherent process, such as CARS, requires the measurement of a coherent transfer function (CFT). Therefore, a precise mathematical framework requires to extract and reconstruct the super-resolution contents into an image with an enhanced resolution. As a result, in practice, extracting the high spatial frequency components of the object due to inherent coherent process of CARS is a complex and process.

3.1.3 Super-resolution SIM by photon statistics evaluation

A subset of super-resolution approaches that do not require non-linearity rely on assessing high-order correlations (or fluctuation) in observed photon statistics to assure super-resolution when using non-Poissonian photon emitters. The sub-diffraction resolution improvement scales with the square root of j, where j is the highest order central moments of the photocounts distribution. Statistical quantum correlation analysis has been used in wide-field and confocal settings [45, 46] with single-photon detectors, as well as the super-Poissonian classical counterpart with linear detectors [47–49]. The latter method is known as Super-resolution Optical Fluctuation Microscopy (SOFI).

The integration of those photon statistics super-resolution methods with SIM has been demonstrated theoretically to provide a much more favourable (linear) scaling, with the correlation order j [50]. The principle has been applied experimentally both for wide field SOFI [51] and for quantum image scanning microscopy [52].

The results of this work are detailed in another publication to be submitted as an extra publication. However, a preprint can be found on arXiv [53].

3.2 Deterministic functional pump/probe techniques

Most deterministic functional pump/probe SRM techniques, which can be summarised as RESOLFT-like methods [54], are based on four building blocks:

1. A switchable detection channel which is usually realised by state population control or modification (in e.g. [55] denoted as "switching states on and off").
2. A detection channel or contrast mechanism, respectively, which usually is the fluorescence emitted by the fluorescence markers.
3. To achieve real superresolution a non-linearity (such as saturation) of the detection signal and the light-molecule interaction is obligatory.
4. Finally, a spatial field shaping (e.g. to provide a donut beam profile) usually of the probe beam is required to enable in combination with the non-linearity a tailoring of the PSF of the microscope imaging.

To achieve label-free SRM schemes many different detection channels as alternatives to fluorescence of marker molecules have been proposed, theoretically analysed and in many cases also experimentally demonstrated including autofluorescence, (transient) absorption, Raman, photothermal detection or photo-modulated reflectivity (cf. [13] and references therein).

As already described in Section 3.1.3, exploitable non-linearities besides saturation, different second order (e.g. SHG or two-photon emission fluorescence 2-PEF) and third order (such as third harmonic generation SHG or CARS) non-linearities have been proposed and demonstrated [32].

Switchable detection channels in a STED-like microscopy scheme can be realised in many four-level systems with suitable state lifetimes and transition rates, respectively. Autofluorescence in the material under test would be of course an easy and self-evident option. However, in most cases the reachable contrast and resolution might be limited and an SRM method based on autofluorescence would require quite flexible pump and probe wavelengths

to adapt to the materials under test. An alternative for technical applications could be alternative marker structures, which could be added as a thin layer on top of the device substrate or included in the substrate material itself, as long as this inclusion does not severely deteriorate the manufacturing process or device performance of the intended nanoscale structure or device. As alternative markers which could be suitable for this approach, e.g. quantum dots or NV centres in artificial diamond have been applied [56, 57]. Alternatively, doping of quartz substrates (as an example) with ions suitable for laser devices, such as Neodymium (Nd) would be promising alternatives to fluorescence marker labelling.

In the following, we will shortly recap some promising approaches for label-free or label-surrogate SRM methods and will discuss their potential for universal SRM-based nanometrology.

3.2.1 STED on NV centres

STED is one of the techniques that produce sub-diffraction resolution by squeezing the PSF through saturated depletion of the excited state of the fluorescence dye [58, 59]. A donut-shaped beam at STED wavelength is used to obtain effective PSF in practice. Here, non-linearity comes from a change in the population of involved states, which is affected by a single-photon process [59]. With this technique, the spatial resolution can be improved down to below 10 nm [60].

3.2.2 SAX

The saturation excitation microscopy technique (SAX) was developed based on extracting saturated emissions [61]. This technique improves the spatial and axial resolution using a confocal microscopy setup by modulating the excitation intensity temporally and detecting the harmonic modulation of the fluorescence signal from the centre of the laser focus [61]. As saturated emission requires high excitation intensity, the photobleaching effect for fluorescence samples is an inevitable problem for imaging. Due to this fact, scattering from individual plasmonic nanostructures is an alternative candidate as a label-free agent in SAX. They provide strong scattering, high photostability, and exceptional localization precision for label-free microscopy [62]. When an individual plasmonic nanoparticle, like a gold nanosphere, is examined for scattering measurements, it shows saturable and reverse saturable absorption. This behaviour occurs near the resonance wavelength of the nanoparticle [63]. Lee et al. indicated that the combination of gold nanoparticles and SAX can improve spatial resolution from a label-free agent [64]. An advantage of this technique is that photobleaching is not common when the intensity of the excitation is high. The lateral and axial resolutions also improved simultaneously, and significant resolution enhancement was observed compared to previous SAX methods using fluorescence markers [64].

3.2.3 SUSI

Enhancement of the surface-to-volume ratio of the plasmonic nanostructures gives rise to increasing the local electric field and providing optical nonlinear interaction, known as nonlinear plasmonics [65]. The nonlinearity allows the control of scattered light from plasmonic nanoparticles by another light source which is called all-optical plasmonic switch. Suppression of scattering imaging (SUSI) is a technique which was developed based on (STED) microscopy systems to create a switch between scattering and non-scattering states of plasmonic nanoparticles for nanoparticle imaging [66]. In this technique, scattering from gold nanoparticles at close to resonance wavelength is controlled by another beam in a confocal microscope setup. A donut-shaped beam at a different wavelength is used to suppress the scattering of particles. When the control beam intensity is increased, the scattering signal of nanoparticles reduces, and a high-resolution image of nanoparticles is obtained. In this way, SUSI can enhance the resolution of gold nanoparticles to $\lambda/9$ [66].

For a range of applications, such as sensors, there is a need for the development of the metrology and imaging of periodic diffractive plasmonic nanostructures. SUSI can be a promising method for imaging this kind of a sample. For spherical plasmonic particles, polarization should not affect the switch process [66]. However, polarization plays an active role in scattering of plasmonic nanostructures. Therefore, a prior study is needed to determine optical properties of the sample such as the precise resonance angle, resonance wavelength and sensitivity of the resonance. In practice, these parameters can be determined using ellipsometry techniques with a standard model and sample.

For this ellipsometric prior study, first, a gold grating with a period of 200 nm, a thickness of 60 nm, and line widths (CD) of 70 nm was prepared. For that 3 nm of Cr followed by 60 nm of gold was deposited on a 150 mm fused silica substrate by thermal evaporation. This is followed by 10 nm of chromium deposited by ion beam sputtering. In the next step, a respective resist pattern is generated using a Vistec 350OS electron beam writer with character projection apertures [67]. This pattern is then transferred to the chromium layer by ion beam sputter etching using argon ions and then into the gold layer using a mixture of argon and oxygen. Finally, the chromium layer is removed by reactive ion etching using chlorine chemistry. The dimensional parameters of the gratings were designed using calculations by the JCMsuite 6.0.10 finite element solver aiming to maximize the variation of the amplitude ratio ($\Psi = \tan^{-1}(|r_p/r_s|)$) and phase shift ($\Delta = \arg(|r_p/r_s|)$) of the reflection coefficients of light polarized parallel (r_p) and perpendicular (r_s) to the plane of incidence. The sample was measured using a Woollam M-2000DI ellipsometer at angles of incidence from 60° to 75°. Figure 4 shows the measured and calculated Ψ and Δ spectra for plane of incidence perpendicular to the grating lines.

The real and imaginary part of the refractive index as a function of wavelength can be obtained through data inversion analysis [68]. Also, sensitive parameters can be identified (not shown here) by analysing the $f'_\Psi = \frac{\partial \Psi}{\partial P}$ and $f'_\Delta = \frac{\partial \Delta}{\partial P}$ derivatives, where P denotes the individual parameters. As a result, essential information such as initial polarization, resonance wavelength, and the sensitivity of resonance

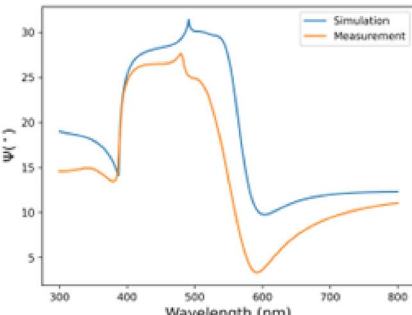

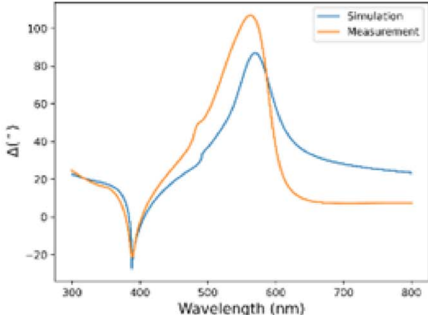

Figure 4. Ψ and Δ ellipsometry spectra calculated by simulation (blue line) and measured (orange line) at an angle of incidence of 70° for CD = 70 nm.

features with respect to design parameters can be obtained before using SUSI for periodic plasmonic nanostructures. Future work would be feasible to investigate the capabilities of the SUSI technique for imaging plasmonic nanostructures in terms of determined parameters with the aid of spectroscopic ellipsometry, which may give us dimensional information about the nanostructure's size and shape.

3.3 Discussion of methods

Among all the super-resolution techniques, STED microscopy is a promising and precise optical far-field technique for nanoscopy. It produces a high-resolution image by modifying the PSF without requiring for any complex mathematical analysis compared to SIM, SUSI, and SAX. For SIM, the post-processing method can be complex for the imaging of a label-free sample. Although SUSI is a promising method for label-free samples as well, it utilizes a complex deconvolution method for coherent emission of samples to improve spatial resolution. For SAX and SSIM, extracting high order nonlinear demodulation components to increase the resolution is a main task. Additionally, in practice, signal-to-noise ratio limits the resolution. In general, the key concept of using STED for a label-free sample is finding a material that can be optically transferred between the four-level system [60].

NV centres are a potential candidate for this task. They can be imaged by STED microscopy with a spatial resolution that is 10–20 times better than the diffraction limit due to high photostability at room temperature [69]. Embedded in diamond substrates, NV centres have great potential as alternative labels in SRM if they exhibit a high density and homogeneous distribution throughout the surface, providing homogeneous fluorescence [58]. A considerable amount of research on NV centres in diamond has investigated the application of NV centres as an individual emitter in quantum information, biosensing, and bioimaging [70]. However, imaging of nanostructures on a NV-centre substrate has not been investigated before.

In Section 4, we will concentrate on investigations of NV centres in artificial diamond as an example four-level system to replace fluorescence labelling.

4 Experimental

4.1 NV centres in artificial diamond

This section describes the preparation and features of the NV test samples:

Diamond nanocrystals (MSY 0-0.25 and 0-0.35) are acquired from Pureon®, with a median size of 125 and 180 nm, respectively. Samples are processed as shown in Figure 5.

Nitrogen impurities are naturally present in NDs with concentrations in the 10–200 ppm range, so that NV centres concentration can be increased by introducing additional vacancies in the lattice with ion irradiation damaging. To this scope, proton irradiation is performed on 125 nm NDs to enhance the concentration of NV centres and maximize their photoluminescence properties. More precisely, samples are dispersed in isopropanol, sonicated, drop-casted on a silicon wafer substrate (~0.5 × 0.5 cm^2) and dried, so forming a ~(30 ± 10) μm thick layer. A 5×5 mm^2 2 MeV H^+ ion beam at the AN2000 accelerator facility of the INFN National Laboratories of Legnaro is employed. Beam current ranged 800–1000 nA. A fluence of 2 × 1016 cm^{-2} is delivered, being in a range of values that were found optimal in order to maximize the concentration of NV centres while preventing quenching effects associated with over-damaging [71]. To evaluate the damage level due to the irradiation, a Monte-Carlo simulation was carried out using SRIM software, following the procedure shown in [71], which proved how 2 MeV protons determine an almost flat damage density across the whole thickness of the NDs layer deposited on the silicon substrate.

High temperature thermal annealing in N_2 flow is then performed for 2 h at 800 °C to promote the formation of NV centres by allowing the generated vacancies to get coupled with the N impurities. The same process is performed on unirradiated NDs for comparison. In this case, the treatment is merely performed to reorganize the crystalline phases and to graphitize the outer layers of amorphous carbon phases surrounding NDs core [72]. Surface purification is finally performed by thermal oxidation in air environment at 500 °C for 8 h. Indeed, in previous work

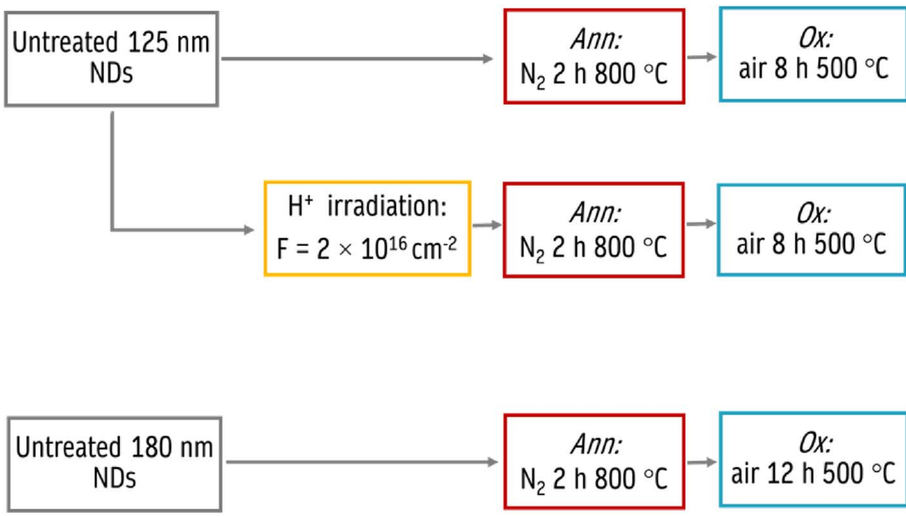

Figure 5. Processes performed on 125 nm and 180 nm in order to optimize their optical properties.

[71], this level of thermal oxidation has proven effective in removing surface quenching phases associated with disordered sp^2/sp^3 carbon and enhancing photoluminescence, while avoiding size reduction and affecting the diamond phases at the basis of the optical properties.

Larger NDs (MSY 0-0.35) with a median size of 180 nm are also analysed in this work. In this case samples are processed with 2 h at 800 °C thermal annealing in N_2 flow, followed by 12 h at 500 °C thermal air oxidation.

Future perspectives

In perspective, luminescent nanodiamonds (LND) are emerging as a powerful tool for advanced optical resolution standards, offering unique capabilities that hold promise for the future of nanoscale imaging and metrology. These nanoparticles, typically less than 100 nm in diameter, can be doped with colour centres (such as nitrogen-vacancy centres) that emit bright and stable fluorescence under various conditions. This luminescence, combined with the exceptional photostability and biocompatibility of nanodiamonds, makes LNDs ideal candidates for high-resolution optical standards. In the future, LNDs are expected to play a critical role in SRM techniques, such as STED microscopy and single-molecule localization microscopy (SMLM). Their luminescence properties enable accurate calibration of imaging systems, allowing for better resolution beyond the diffraction limit of light. Furthermore, LNDs can serve as a reference for quantifying spatial resolution, validating imaging algorithms, and correcting optical aberrations in these advanced microscopes. As ion-beam-based fabrication techniques advance, it is becoming increasingly possible to produce luminescent nanodiamonds with tailored optical properties and precisely engineered shapes and sizes. This customization could lead to the creation of a new class of optical standards with unparalleled specificity and adaptability for various imaging modalities.

4.2 Wide-field Imaging with Super-resolution Enabled by Raman Scattering (WISERS)

The above scheme has been implemented to acquire label-free imaging using Raman signals [73, 74].

The spatial frequency with wave-vector k_s was projected on the sample plane at three phase angles and three orientations. The super-resolution image was reconstructed using the fairSIM plug-in in ImageJ [75]. An implanted diamond sample (c.f. Sect. 4.1) was used that include NV vacancies in the nanoscale domains of sp^3 hybridised diamond clusters surrounded by sp^2 hybridised graphitic layer [76]. The signal from the sample appeared as a convoluted peak around 1410 cm^{-1} which is likely to be a combination of the 1332 cm^{-1} diamond, the PL signal and the D-peak from graphitic carbon.

The results are shown in Figure 6. Hyperspectral image was acquired using Fourier-transform interference method using birefringent crystals. A representative spectrum acquired using the interferometer is compared with that obtained using a monochromator (Fig. 6a). A wide-field image acquired using wide-field illumination and collection using a narrow band filter is shown in Figure 6b, that shows a distribution of the emitting centres although these could not be resolved clearly. The same area was subsequently imaged using a narrow band filter and structured illumination with line spacing of 1200 nm projected on the sample plane (Fig. 6c). Nine images were acquired with three phase angles and three orientations of the lines, and the super-resolution image was reconstructed. Clearly, there is a significant improvement in clarity of the image. The improvement is due to the expansion of the total k-vector ($k_0 + k_s$) that allowed to capture the high frequency features of the sample. The clarity of the image improved further by acquiring the imaging using hyperspectral imaging. This improvement is highlighted in Figures 6b1–6d1 which are the zoomed-in regions of the marked areas in the corresponding Figures 3b–3d. The intensity profiles

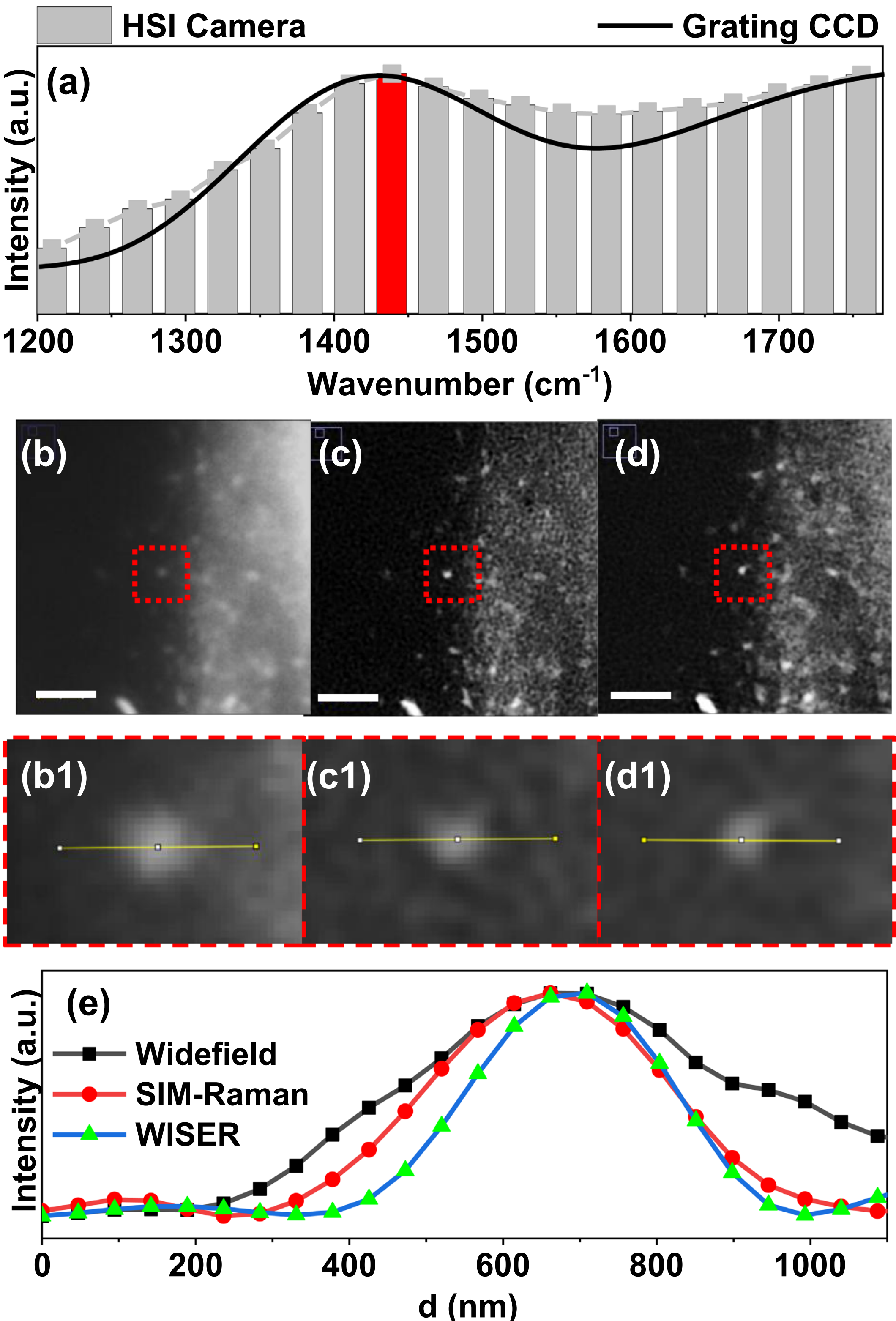

Figure 6. (a) Representative spectra from the hyperspectral image and a monochromator. (b) Wide-field image acquired using a narrow band filter by wide-field illumination without structured light. (c) Structured illumination image acquired using a narrow band filter with illumination using structured light. (d) Structured illumination image using hyperspectral imaging. (b1–d1) show the corresponding zoomed-in image of the marked areas in (b–d). (e) The intensity profile along the line shown in image b1–d1.

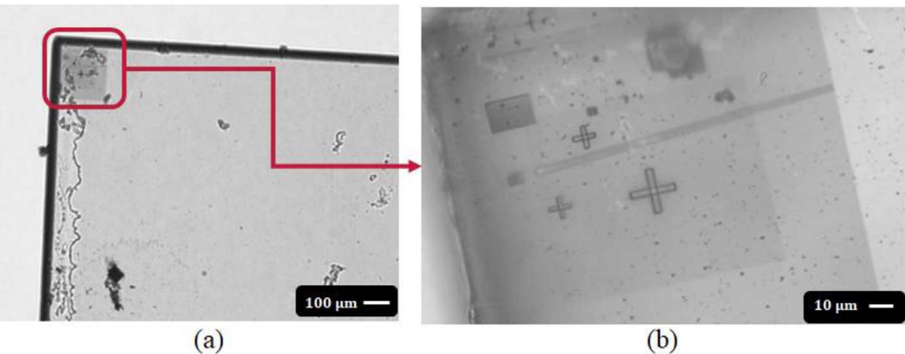

Figure 7. Light microscope image of the NV centres substrate. (a) Patterns fabricated in the corner of the sample are shown in the red rectangle. (b) Different shapes of fabricated patterns on the NV-centre substrate.

along the line in Figures 6b1–6d1 are shown in Figure 6e. It is evident that the structured illumination image acquired using hyperspectral imaging shows the best spatial resolution. An improvement of 1.6 times was achieved compared to the diffraction limited spatial resolution. The set up is now fully optimised with the structured illumination line spacing. With diffraction limited line spacing, a spatial resolution improvement of 2 times would be achievable.

4.3 NV centres as test four-level system for STED-like SRM

In this section, first, we investigated the distribution of NV centres in a diamond substrate by measuring photoluminescence (PL) spectra for the existence of NV centres in the substrate as well as their homogeneities and for comparing the spectral resolution as proposed by Balasubramanian et al. [70]. Next, we imaged two random structures with a separation distance of 330 nm, and a cross-shaped pattern with 2.1 µm in size on the surface of a substrate with the NV centres in STED and confocal mode using a STED microscopy system. As a result of our tests, STED mode already provided higher-resolution images of the structures on the substrate surface than the confocal mode.

The sample is an artificial diamond substrate with embedded NV centres (cf. Sect. 4.1). The dimensions of the sample are $3 \times 3 \times 0.5$ mm^3. The fabricated patterns in the sample corner were designed and fabricated by lithography (Fig. 7). To evaluate the PL spectrum of the sample, we used Raman spectroscopy in PL mode for different positions as well as from the bottom side of the sample.

We used a STED microscopy system (Abberior Instruments, Göttingen, Germany) to obtain high-resolution NV-centre images. The STED microscope is equipped with pulsed laser lines with wavelengths of 561 nm and 775 nm for excitation and saturation depletion of the excitation state, respectively. A vortex phase plate is inserted into the optical path of the 775 nm laser to generate a donut-shaped beam. Both laser beams are overlapped and focused onto the sample using an oil-immersion objective with NA = 1.4. Finally, the emission signal of the NV-centre is recorded under reflection confocal detection (Fig. 8).

Theoretically, there are two modes to investigate and find the resolution for STED techniques. Based on using a pulsed or a CW laser, these modes are called pulsed mode and CW mode [77]. For pulse mode, the lateral resolution is given by [60]:

$$\Delta r = \frac{d_c}{\sqrt{1 + {d_c}^2 \left(\frac{\beta \pi n}{\lambda}\right)^2 \xi}} \overset{\xi \gg 1}{\Longrightarrow} \Delta r \cong \frac{\lambda}{\beta \pi n}\sqrt{\frac{1}{\xi}}, \tag{1}$$

where $\xi = \frac{I_m}{I_{sat}}$ is the saturation factor, I_{Sat} is the saturation intensity (half of the population is quenched at the STED saturation intensity), I_{m} is the maximum intensity at the donut crest, d_{c} is the full width at half maximum (FWHM) of the confocal PSF, n is the refractive index, λ is the STED wavelength, and β quantifies the steepness of the minimum intensity.

We adjusted a set of practical parameters as shown in Table 1 which are defining for the STED microscopy system. Depending on the type of sample, these parameters help us obtain an image with high contrast and resolution. In the next section, we will discuss the effect of each parameter on the imaging of the patterns.

4.3.1 Measurement of photoluminescence spectrum on NV centre samples

To obtain the PL spectrum of the sample, Raman spectroscopy in PL mode was used. The range of wavelengths was selected between 550 and 800 nm. To determine the homogeneity of the NV-centre population in the sample, five different positions of the sample were chosen to compare the similarity of their spectrum (see Fig. 9). For each position, the optical parameters of the setup were kept constant. The defect excited by green light (532 nm) and the power of the laser was adjusted to 5 mW. Moreover, other laser powers were tested. The chosen power had a good signal-to-noise ratio without any harmful effect on the sample. An objective with 50× magnification was used for focusing the laser beam on the sample. The signal from the other side of the sample was obtained to determine the presence of NV centres on the bottom side of the sample.

PL spectra for different positions on the sample surface as well as from the bottom of the sample were measured

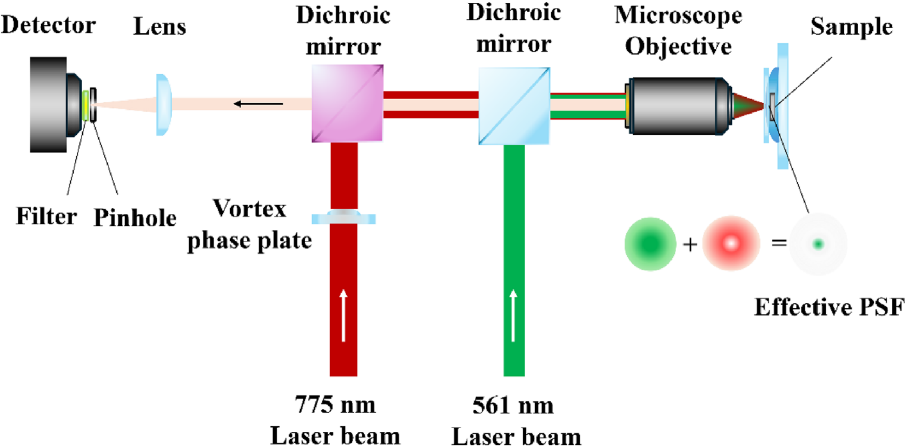

Figure 8. Schematic of the STED microscope setup.

Table 1. Set of parameters adjusted for STED microscopy in practice.

Parameters	Definition
Pixel size	Dimension of each pixel of the image
Pinhole size	1 A.U.
Dwell time	The time during that light is detected from each volume element
Line accumulation	Repeating each line including several pixels (# pixels)
Excitation power %	Reported based on percentage of Excitation laser power
STED power %	Reported based on percentage of STED laser power
Excitation wavelength	561 nm
STED wavelength	775 nm
Frame size	Dimension of each image

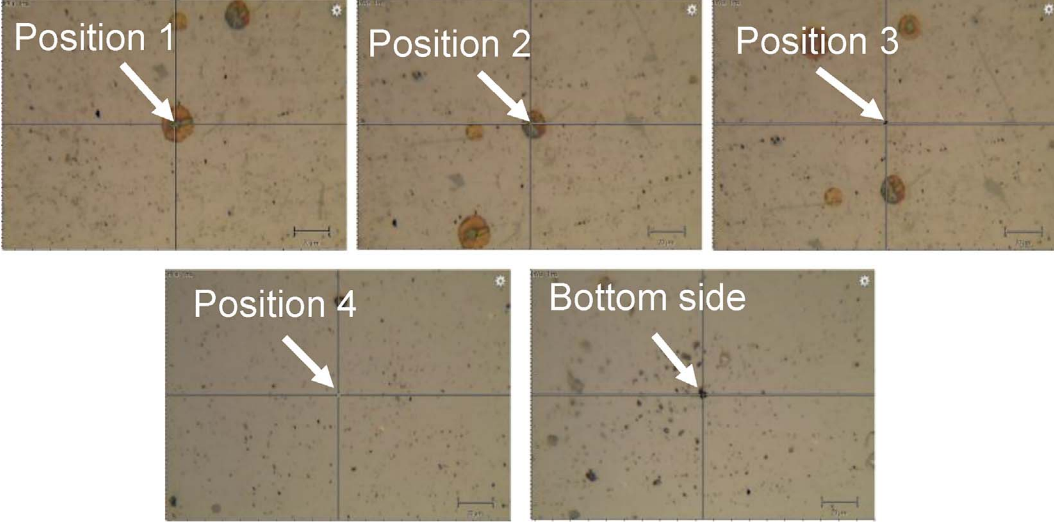

Figure 9. Five different positions of the sample for obtaining PL spectra.

and are depicted in Figure 10. The PL measurements show that there are two peaks at $\lambda = 575$ nm and $\lambda = 637$ nm for the neutral charge state (NV^0) and the negative charge state (NV^-) of the NV centres, respectively.

These peaks indicate a zero-phonon line (ZPL) at room temperature where purely electronic transition occurs. The spectra indicate a broad fluorescence emission in the spectral range from about 550–800 nm, with a maximum

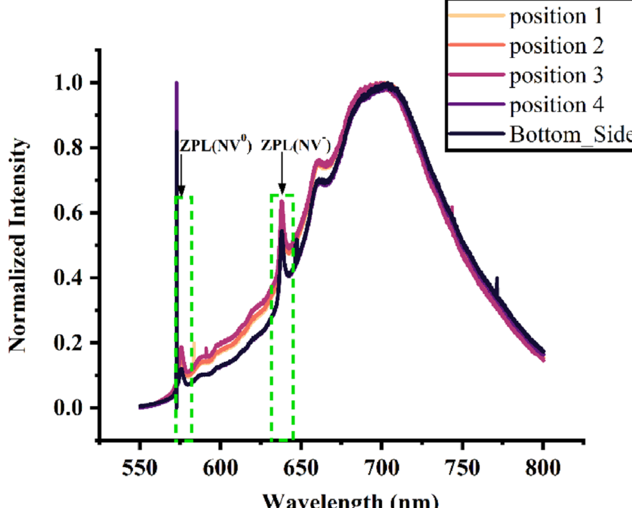

Figure 10. PL spectra for different positions on the sample surface as well as the bottom of the sample. Fluorescence emission from NV centres shows two peaks at wavelengths 575 nm (NV^0) and 637 nm (NV^-) for different positions. Green dotted boxes show ZPL for (NV^0) and (NV^-) separately.

around 700 nm. The result is in good agreement with the typical emission wavelength spectrum of NV centres [70], showing that the NV centres are distributed evenly over the sample.

4.3.2 STED measurement

In the first step, we tried to find the optimum excitation and STED power, expressed as a percentage of the maximum excitation and STED laser power, to image the patterns of the sample. The maximum pulsed STED and excitation laser powers are 3 W and 150 μW at f_{rep} = 40 MHz respectively. Initially, we imaged a random feature on the substrate. Based on the PL spectrum, a wavelength range between 600 nm and 700 nm was selected to collect the fluorescence emission with the detector. Further parameters are listed in Table 2.

Figure 11 indicates the image of the features in confocal and STED modes. The arrow in Figure 11 indicates each feature. Figure 12 shows the intensity profiles of a cross-section through the features. There is a drop in fluorescence emission intensity around the border of the features in STED mode. The dotted lines in the STED mode diagram indicate areas where the intensity drops to zero. These areas are not clear in the confocal mode diagram compared to the STED mode diagram. Thus, two features with a separation distance of 330 nm can be resolved in STED mode. Moreover, our result shows that the border of the features have a proper contrast in STED mode.

Although high line accumulation improves the signal-to-noise ratio, it causes a slow recording of the image. For 14 lines of accumulation in a frame size of 4.5 × 2 μm^2, we observed a slight stage drift that caused changes in the focal plane during data acquisition. Additionally, at the determined laser power, we found that both the excitation and STED powers were too high, resulting in damage to several areas of the sample. Therefore, we sought to modify a set of the proper parameters for the STED microscope system to increase contrast and resolution without any harmful effect on sample.

For the next measurement, we recorded images of a cross-shaped pattern on the NV centres substrate in two cases, based on changes to the optimum STED parameters. For both cases, we used similar parameter values except for the pixel size. To prevent damage to the sample, we reduced the excitation and STED power to 3% and 5% of their respective laser powers. To increase the speed of image recording, we decreased the line accumulation value to one. The pinhole size, excitation wavelength, STED wavelength, and frame size are the same for both cases (see Table 3).

Case I

The image of the cross-shaped pattern in both confocal and STED modes was obtained using the determined values of Case I in Table 3 (see Fig. 13). The arrow in Figure 13 indicates the location where the intensity profile was measured. Figure 14 shows the intensity profiles of the yellow line through the cross-shaped pattern. There is a drop in fluorescence emission intensity around the borders of the features in STED mode. The dotted lines in the STED mode diagram indicate the area where the intensity drops to zero. Again, in the STED image, the borders of the pattern are evident, whereas these areas are not clear in the confocal mode diagram.

Case II

Figure 15 exhibits images of the cross-shaped pattern in both confocal and STED modes for determined values of Case II in Table 3. The arrow in the Figure 15 indicates the location where the intensity profile was measured. Figure 16 shows the intensity profiles of the yellow line through the cross-shaped pattern. The fluorescence emission intensity in Case II falls sharply around the borders of the pattern compared to Case I. The dotted lines in the STED mode diagram indicate area where the intensity drops to zero. The width of the area is 2.1 μm. This result shows that reducing the pixel size of the image while maintaining the same dwell time (20 μs) helps us record a high-resolution image of the pattern. However, the scanning time in Case II increases two times compared to Case I.

5 Discussion of concepts for universal and versatile label-free-SRM metrology tool(s)

As might be obvious from the number of different label-free SRM methods we considered and investigated for the goal to develop and realise practical and (as much as possible) universal label-free SRM methods applicable in dimensional nanometrology, an optimum solution for this challenge might not exist, but according to the intended application, different methods might be required. Usually, the investigated materials and structures will not offer suitable

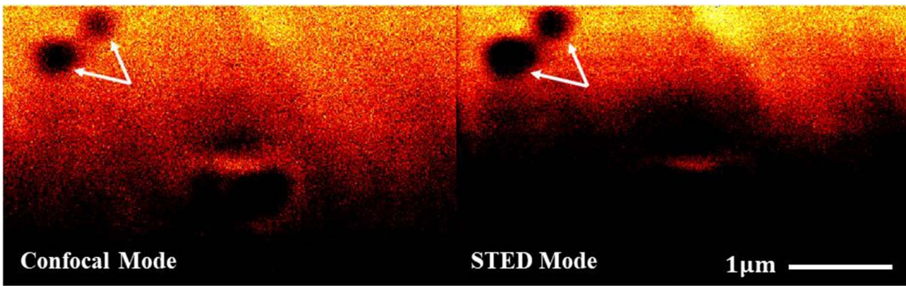

Figure 11. Image of the random features in confocal mode (a) and STED mode (b).

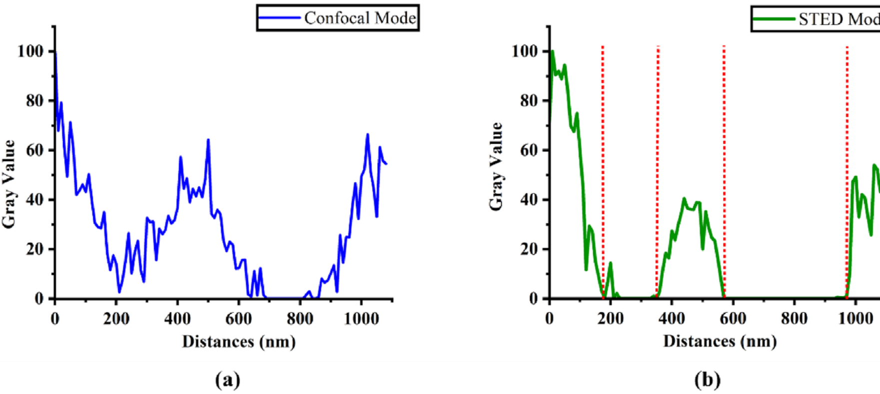

Figure 12. Intensity profile of the random features for confocal mode (a) and STED mode (b). The dotted lines in the STED mode diagram show the approximate border of each feature.

Table 2. Parameters for imaging a random structure on the NV centres substrate.

Parameters	Values
Pixel size	10 nm
Pinhole size	1 A.U.
Dwell time	10 µs
Line accumulation	14
Excitation power	25%
STED power	25%
Excitation wavelength	561 nm
STED wavelength	775 nm
Frame size	4.5 × 2 µm^2

Table 3. Parameters for imaging the cross-shaped pattern on the NV centres substrate for two cases.

Parameters	Values for Case I	Values for Case II
Pixel size	20 nm	10 nm
Pinhole size	1 A.U.	1 A.U.
Dwell time	20 µs	20 µs
Line accumulation	1	1
Excitation power	2%	2%
STED power	5%	5%
Excitation wavelength	561 nm	561 nm
STED wavelength	775 nm	775 nm
Frame size	15 × 15 µm^2	15 × 15 µm^2

switchable detection channel systems, which might be exploited for non-linear pump-probe SRM methods such as STED or ground state depletion GSD. Positive exceptions might be silicon-based nanostructures, when the plasma dispersion effect can be exploited [78] or other label-free SRM methods based on plasmonic scattering suppression like in the SAX and SUSI methods described in Section 3. An alternative with a potentially broader application potential might be provided by nonlinear photo-modulated reflectivity [79].

There exist many applications in nanotechnologies which should be suitable to implement thin inorganic extra layers on top of the substrate or ion dopants within a transparent substrate with alternatives to fluorescence markers, such as NV centres in artificial diamond, quantum dots or Nd-ions, which can be exploited relatively straight forward for RESOLFT-like SRM.

In applications where such extra-layers or dopants are not acceptable and where no other alternatives such as

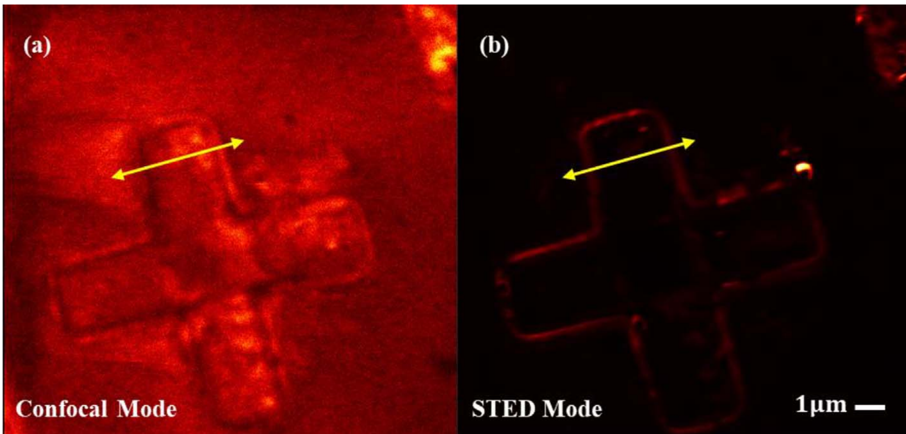

Figure 13. Image of the cross in confocal mode (a) and STED mode (b).

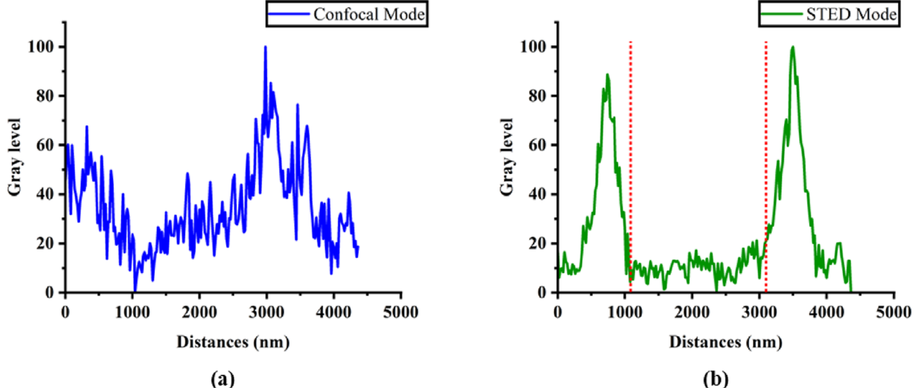

Figure 14. Intensity profile of the yellow arrow in image of the cross -shaped pattern for confocal mode (a) and STED mode (b). The dotted lines in diagram (b) show the border of the pattern based on the drop of intensity in STED mode.

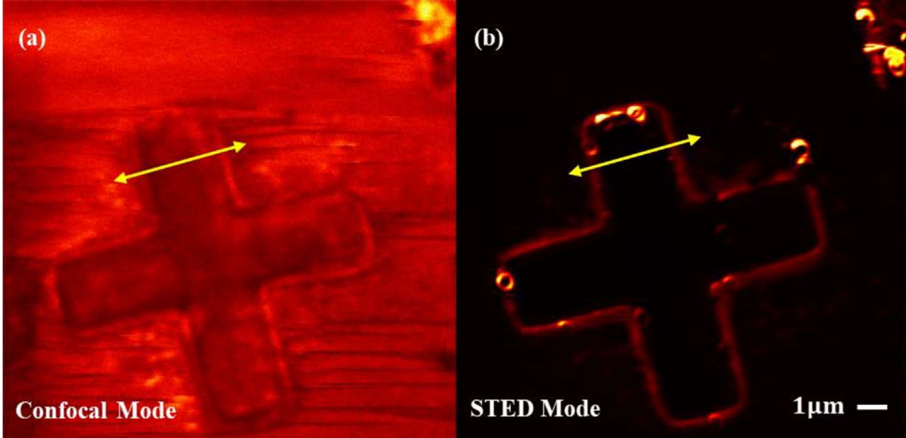

Figure 15. Image of the cross-shaped pattern in confocal mode (a) and STED mode (b).

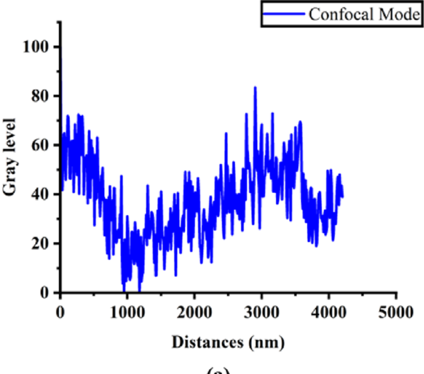

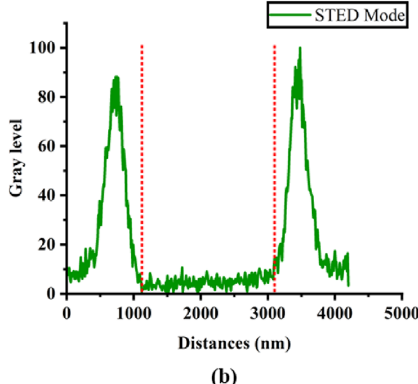

Figure 16. Intensity profile of the yellow arrow in image of the cross for STED mode (a) and confocal mode (b). The dotted lines in (b) show the border of the pattern based on the drop of intensity in STED mode.

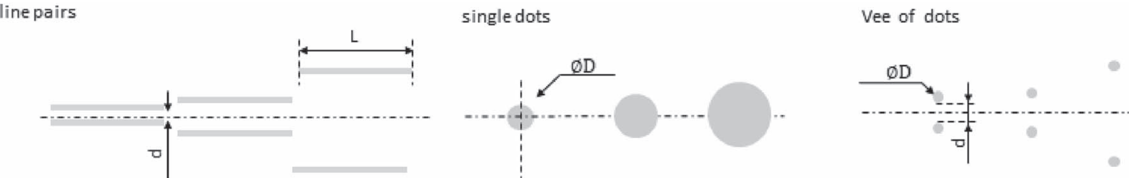

Figure 17. Design of planned possible reference structures.

plasmonic scattering or other alternative detection channel switching schemes can be realized, so that pump-probe SRM schemes are not applicable, non-linear SIM methods will be the remaining options. The possible switch-able and non-linear detection schemes described in Section 3 appear to be quite universally applicable. In combination with (coherent or incoherent) Raman scattering, a chemical imaging can increase the imaging contrast and performance.

6 Conclusion and outlook

In this publication we presented an overview about research performed by several partners within a European research project on the way to realise universal label-free SRM methods suitable for reliable optical dimensional nanometrology as an imaging complement to well-proven non-imaging OCD methods and a fast and contamination free alternative to nano-imaging methods such as AFM or SEM, which are required to characterise individual and single structures and defects.

We provided a short review on the performance and applications of the investigated linear and non-linear SIM and novel pump-probe SRM techniques including surface plasmon resonances (SPR) assisted Raman, coherent multi-photon-Raman, and STED-like methods.

In this work, we have shown investigations of though-focus microscopy, a method to improve nanoscale sensitivity in classical microscopy by adding phase information to the analysis. Different novel schemes to apply SIM methods have been investigated based e.g. on photon statistics evaluation and in a combination of structured illumination Raman and hyperspectral imaging (WISER), both showing quite promising results.

Additionally, we investigated the NV centres in different artificial diamond as a promising candidate for super-resolution imaging due to its high fluorescence stability. Desired patterns were fabricated on an NV-centre substrate. By examining photoluminescence spectra, we found that NV centres in the substrate have a uniform distribution and sufficient spectral resolution. We imaged the fabricated pattern on the NV-centre substrate using both STED and confocal modes. We determined the optimum experimental parameters for imaging our sample with STED microscopy. Compared to confocal mode, STED mode provides better contrast at the borders of features and patterns. Therefore, STED mode is a promising tool for dimension measurement of nanostructures on substrates with NV centres. While an increase in STED power is often associated with improved resolution, our sample exhibited damage points at STED power levels above 5%. Different values of STED power could be used to investigate this further by preparing an NV-centre substrate with smaller-sized patterns as well as compatible with a high power of the STED laser.

To go beyond super-resolution imaging and extend it to a quantitative dimensional metrology tool, as stated in the introduction, some requirements must be addressed.

Beside a stable and reproducible measurement system and a very good understanding of the probe-sample interaction, which usually comes along with a detailed, reliable and

realistic modelling capability of the whole measurement process and system, the question of the traceability of the measurements is of highest importance for dimensional metrology. A straightforward method to achieve and prove traceability is the development, calibration and successful application of traceable reference standards to the SRM-based metrology method used [28]. The nanodiamond NV-centre material is a very promising option to realise suitable test structures for STED-like SRM. Low density NV-centre samples, where individual centres can be identified are excellent samples to characterise the PSF and with it the resolution of the method. And they can be arranged stochastically or deterministically as two-dot samples with calibrated distances to be useful for direct resolution measurements of the SRM.

For a planned alternative, high quality calibration grating structures may be utilized. These elements are fabricated by first deposition a chromium hard mask onto a silicon wafer by means of ion beam sputter deposition (Ionfab 300LC by OIPT) [80]. In a next step, HMDS adhesion promoter and 100 nm of electron beam sensitive OEBR-CAN038 AE 2.0CP (Tokyo Ohka Kogyo Co. LTD) is applied. This is subsequently patterned by a Vistec 350OS electron beam writer with character projection apertures [68]. Then, the pattern is transferred into the silicon substrate using the chromium as a hardmask by means of inductive coupled plasma etching (SI500C by Sentech Instruments GmbH). The remaining hardmask is removed and the samples are diced. The grating parameters such as period, linewidth and height etc. will then be calibrated by a traceable AFM [81]. Finally, a polymer layer is formed on top of the structures by means of spincoating. Into this polymer low concentration of nanodiamond powder containing NV centres is embedded, enabling STED measurements.

Potential reference structures for the calibration of the respective metrology systems are shown in Figure 17. Those target structures have been already manufactured, but are not yet treated with the nanodiamond layer. It contains line pairs with different distances, single dots with different diameters and pairs of dots with different distances. The later allow to directly assess the resolution limits.

Funding

This project (20FUN02 “POLight”) has received funding from the EMPIR program co-financed by the Participating States and from the European Union’s Horizon 2020 research and innovation program.

Conflicts of interest

The authors declare that they have no competing interests to report.

Data availability statement

This work has been fully performed within the EURAMET project 20FUN02 POLight and EURAMET projects all are in full agreement with the FAIR data principle. All research data associated with this article are available on request from the authors.

Author contribution statement

The work is a result of contributions from all authors. The work followed initial conceptualisation by Stefanie Kroker, Deb Roy and Bernd Bodermann. Mohammad Nouri and Bernd Bodermann collected the different partner input and drafted the basic manuscript. The samples have been designed, manufactured and provided by Paolo Olivero, Pietro Apra and Thomas Siefke, who also significantly contributed to the discussion of future reference standard samples in the conclusions. Ivano Ruo-Berchera significantly supported the design of different structured illumination creation and provided the work on super-resolution SIM by photon statistics evaluation (Sect. 3.1.3). Himanshu Tyagi and Deb Roy developed and performed the wide-field Raman SRM with hyperspectral extension, while Astrid Tranum Rømer and Poul Erik Hansen developed, performed and analysed measurements with through focus microscopy. Deshabrato Mukherjee and Peter Petrik provided the pre-investigations and measurements for plasmonic resonances required for the SUSY SRM technique (Sect. 3.2.3). Miroslav Valtr provided traceable measurements and dimensional characterisations of the different test samples used and strongly supported the measurement uncertainty evaluation processes and discussions. Tim Käseberg and Mohammad Nouri performed and analysed the STED investigations on the NV centre samples and together with Stefanie Kroker and Bernd Bodermann concepts for universal and versatile label-free-SRM and future follow-up work have been discussed.

References

1 Bunday B, Orji N, Allgair J, High volume manufacturing metrology needs at and beyond the 5 nm node, *Proc. SPIE* **11611**, 116110F (2021). https://doi.org/10.1117/12.2584555.
2 IEEE International Roadmap for Devices, Systems, *Metrology* (Institute of Electrical and Electronics Engineers, 2023). https://doi.org/10.60627/ff6x-d213.
3 Diebold AC, Antonelli A, Keller N Perspective: optical measurement of feature dimensions and shapes by scatterometry, *Apl. Materials.* **6**, 058201 (2018). https://doi.org/10.1063/1.5018310.
4 Bodermann B, Diener A, Scholze F, Heidenreich S, Soltwisch V, Wurm M, in: *Proceedings of Frontiers of Characterization and Metrology for Nanoelectronics*, edited by Astratov D Seiler, Z Ma(McDonald B, 2017), p. 70. https://www.nist.gov/sites/default/files/documents/2017/03/22/2017fcmncomplete.pdf.
5 Masters BR, *Superresolution optical microscopy. Springer series in optical sciences*, (Springer, 2020). https://doi.org/10.1007/978-3-030-21691-7.
6 Rockstuhl C, Marki I, Scharf T, Salt M, Peter Herzig H, Dandliker R, High resolution interference microscopy: a tool for probing optical waves in the far-field on a nanometric length scale, *Curr. Nanosci.* **2**, 337 (2006). https://doi.org/10.2174/157341306778699383.
7 Zhang T, Ruan Y, Maire G, Sentenac D, Talneau A, Belkebir K, Chaumet PC, Sentenac A, Full-polarized tomographic diffraction microscopy achieves a resolution about one-fourth of the wavelength, *Phys. Rev. Lett.* **111**, 243904 (2013). https://doi.org/10.1103/PhysRevLett.111.243904.
8 Ehret G, Bodermann B, Mirandé W, Quantitative linewidth measurement down to 100 nm by means of optical dark-field microscopy and rigorous model-based evaluation, *Meas. Sci. Technol.* **18**, 430 (2007). https://doi.org/10.1088/0957-0233/18/2/S15.

9 Bodermann B, Ehret G, Endres J, Wurm M, Optical dimensional metrology at Physikalisch-Technische Bundesanstalt (PTB) on deep sub-wavelength nanostructured surfaces, *Surf. Topogr. Metrol. Prop.* **4**, 024014 (2016). https://doi.org/10.1088/2051-672X/4/2/024014.

10 Silver RM, Barnes BM, Attota R, Jun J, Stocker M, Marx E, Patrick HJ, Scatterfield microscopy for extending the limits of image-based optical metrology, *Appl. Opt.* **46**, 4248 (2007). https://doi.org/10.1364/AO.46.004248.

11 Attota R, Silver R, Barnes BM, Optical through-focus technique that differentiates small changes in line width, line height, and sidewall angle for CD, overlay, and defect metrology applications, *Proc. SPIE* **6922**, 146 (2008). https://doi.org/10.1117/12.777205.

12 Schermelleh L, Ferrand A, Huser T, Eggeling C, Sauer M, Biehlmaier O, Drummen GP, Super-resolution microscopy demystified, *Nat. Cell Biol.* **21**, 72 (2019). https://doi.org/10.1038/s41556-018-0251-8.

13 V, *Label-free super-resolution microscopy* (Springer, 2019). https://doi.org/10.1007/978-3-030-21722-8.

14 Gustafsson MG, Agard DA, Sedat JW, Sevenfold improvement of axial resolution in 3D wide-field microscopy using two objective-lenses, *Proc. SPIE* **2412**, 147 (1995). https://doi.org/10.1117/12.205334.

15 Gustafsson MG, Surpassing the lateral resolution limit by a factor of two using structured illumination microscopy, *J. Microsc.* **198**, 82 (2000). https://doi.org/10.1046/j.1365-2818.2000.00710.x.

16 Gustafsson MG, Nonlinear structured-illumination microscopy: wide-field fluorescence imaging with theoretically unlimited resolution, *Proc. Natl. Acad. Sci.* **102**, 13081 (2005). https://doi.org/10.1073/pnas.0406877102.

17 Rego EH, Shao L, Macklin JJ, Winoto L, Johansson GA, Kamps-Hughes N, Davidson MW, Gustafsson MG, Nonlinear structured-illumination microscopy with a photoswitchable protein reveals cellular structures at 50-nm resolution, *Proc. Natl. Acad. Sci.* **109**, E135 (2012). https://doi.org/10.1073/pnas.1107547108.

18 Hell SW, Wichmann J, Breaking the diffraction resolution limit by stimulated emission: stimulated-emission-depletion fluorescence microscopy, *Opt. Lett.* **19**, 780 (1994). https://doi.org/10.1364/OL.19.000780.

19 Klar TA, Hell SW, Subdiffraction resolution in far-field fluorescence microscopy, *Opt. Lett.* **24**, 954 (1999). https://doi.org/10.1364/OL.24.000954.

20 Betzig E, Patterson GH, Sougrat R, Lindwasser OW, Olenych S, Bonifacino JS, Davidson MW, Lippincott-Schwartz J, Hess HF, Imaging intracellular fluorescent proteins at nanometre resolution", *Science* **313** (2006) 1642. https://doi.org/10.1126/science.1127344.

21 Rust MJ, Bates M, Zhuang X, Sub-diffraction-limit imaging by stochastic optical reconstruction microscopy (STORM), *Nat. Methods* **3**, 793 (2006). https://doi.org/10.1038/nmeth929.

22 https://www.euramet.org/research-innovation/research-empir.

23 https://www.ptb.de/empir2021/polight/home/https://www.euramet.org/research-innovation/search-research-projects/details/project/pushing-boundaries-of-nano-dimensional-metrology-by-light.

24 Rayleigh, XXXI. Investigations in optics, with special reference to the spectroscope, *London Edinburgh Philos. Mag. & J. Sci.* **8**, 261 (1879). https://doi.org/10.1080/14786447908639684.

25 Hansen PE, Pahl T, Fu L, Rømer AT, Rosenthal F, Siaudinyte L, Reichelt S, Lehmann P, Karamehmedović M, Digital twins for 3D confocal microscopy, *Proc. SPIE Int. Soc. Opt. Eng.* **12997**, 12997 (2024). https://doi.org/10.1117/12.3016808.

26 Attota RK, Through-focus or volometric type of imagingin methods: a review, *J. Biomed. Opt.* **23**, 070901 (2018). https://doi.org/10.1117/1.JBO.23.7.070901.

27 Pawley J (Ed.), *Handbook of biological confocal microscopy* (Plenum, 1995).

28 Raab M, Jusuk I, Molle J, Buhr E, Bodermann B, Bergmann D, Bosse H, Tinnefeld P, Using DNA origami nanorulers as traceable distance measurement standards and nanoscopic benchmark structures, *Sci. Rep.* **8**, 1780 (2018). https://doi.org/10.1038/s41598-018-19905-x.

29 Hofmann M, Eggeling C, Jakobs S, Hell SW, Breaking the diffraction barrier in fluorescence microscopy at low light intensities by using reversibly photoswitchable proteins, *Proc. Natl. Acad. Sci.* **102**, 17565 (2005). https://doi.org/10.1073/pnas.0506010102.

30 Lu J, Min W, Conchello JA, Xie XS, Lichtman JW, Super-resolution laser scanning microscopy through spatiotemporal modulation, *Nano Lett.* **9**, 3883 (2009). https://doi.org/10.1021/nl902087d.

31 Käseberg T, Siefke T, Kroker S, Bodermann B, Inverted plasmonic lens design for nanometrology applications, *Meas. Sci. Technol.* **31**, 074013 (2020). https://doi.org/10.1088/1361-6501/ab7e6b.

32 Karamehmedović M, Scheel K, Listov-Saabye Pedersen F, Villegas A, Hansen PE, Steerable photonic jet for super-resolution microscopy, *Opt. Express* **30**, 41757 (2022). https://doi.org/10.1364/OE.472992.

33 Parodi V, Jacchetti E, Osellame R, Cerullo G, Polli D, Raimondi MT, Nonlinear optical microscopy: From fundamentals to applications in live bioimaging, *Front. Bioeng. Biotechnol.* **8**, 585363 (2020). https://doi.org/10.3389/fbioe.2020.585363.

34 Campagnola PJ, Clark HA, Mohler WA, Lewis A, Loew LM, Second-harmonic imaging microscopy of living cells, *J. Biomed. Opt.* **6**, 277 (2001). https://doi.org/10.1117/1.1383294.

35 Rehberg M, Krombach F, Pohl U, Dietzel S, Label-free 3D visualization of cellular and tissue structures in intact muscle with second and third harmonic generation microscopy, *PLoS One* **6**, e28237 (2011). https://doi.org/10.1371/journal.pone.0028237.

36 Huttunen MJ, Abbas A, Upham J, Boyd RW, Label-free super-resolution with coherent nonlinear structured-illumination microscopy, *J. Opt.* **19**, 085504 (2017). https://doi.org/10.1088/2040-8986/aa792d.

37 Cheng JX, Xie XS, Coherent anti-Stokes Raman scattering microscopy: instrumentation, theory, and applications, *J. Phys. Chem. B* **108**, 827 (2004). https://doi.org/10.1021/jp035693v.

38 Greve M, Bodermann B, Telle HR, Baum P, Riedle E, High-contrast chemical imaging with gated heterodyne coherent anti-Stokes Raman scattering microscopy, *Appl. Phys. B* **81**, 875 (2005). https://doi.org/10.1007/s00340-005-1979-y.

39 Cheng JX, Volkmer A, Xie XS, Theoretical and experimental characterization of coherent anti-Stokes Raman scattering microscopy, *J. Opt. Soc. Am. B* **19**, 1363 (2002) 1375. https://doi.org/10.1364/JOSAB.19.001363.

40 Zhang C, Aldana-Mendoza JA (2021) Coherent Raman scattering microscopy for chemical imaging of biological systems, *J. Phys. Photonics* **3**, 032002. https://doi.org/10.1088/2515-7647/abfd09.

41 Greve M, Bodermann B, Telle HR, Baum P, Riedle E, Gated heterodyne coherent anti-Stokes Raman scattering for high-contrast vibrational imaging, *Optical Measurement Systems for Industrial Inspection IV, SPIE* **5856**, 41 (2005). https://doi.org/10.1117/12.612555.

42 Boyd RW, *Nonlinear optics*, 4th edn (Elsevier, 2020).

43 Park JH, Lee SW, Lee ES, Lee JY, A method for super-resolved CARS microscopy with structured illumination in two dimensions, *Opt. Express* **22**, 9854 (2014). https://doi.org/10.1364/OE.22.009854.

44 Hajek KM, Littleton B, Turk D, McIntyre TJ, Rubinsztein-Dunlop H, A method for achieving super-resolved widefield CARS microscopy, *Opt. Express* **18**, 19263 (2010). https://doi.org/10.1364/OE.18.019263.

45 Schwartz O, Levitt JM, Tenne R, Itzhakov S, Deutsch Z, Oron D, Superresolution microscopy with quantum emitters, *Nano Lett.* **13**, 5832 (2013). https://doi.org/10.1021/nl402552m.

46 Gatto Monticone D, Katamadze K, Traina P, Moreva E, Forneris J, Ruo-Berchera I, Olivero P, Degiovanni IP, Brida G, Genovese M, Beating the Abbe diffraction limit in confocal microscopy via nonclassical photon statistics, *Phys. Rev. Lett.* **113**, 143602 (2014). https://doi.org/10.1103/PhysRevLett.113.143602.

47 Dertinger T, Colyer R, Iyer G, Weiss S, Enderlein J, Fast, background-free, 3D super-resolution optical fluctuation imaging (SOFI), *Proc. Natl Acad. Sci.* **106**, 22287 (2009). https://doi.org/10.1073/pnas.0907866106.

48 Cevoli D, Vitale R, Vandenberg W, Hugelier S, Van den Eynde R, Dedecker P, Ruckebusch C, Design of experiments for the optimization of SOFI super-resolution microscopy imaging, *Biomed. Opt. Express* **12**, 2617 (2021). https://doi.org/10.1364/boe.421168.

49 Pawlowska M, Tenne R, Ghosh B, Makowski A, Lapkiewicz R, Embracing the uncertainty: the evolution of SOFI into a diverse family of fluctuation-based super-resolution microscopy methods, *J. Phys. Photonics* **4**, 012002 (2021). https://doi.org/10.1088/2515-7647/ac3838.

50 Classen A, von Zanthier J, Scully MO, Agarwal GS, Superresolution via structured illumination quantum correlation microscopy, *Optica* **4**, 580 (2017). https://doi.org/10.1364/OPTICA.4.000580.

51 Descloux AC, Grußmayer KS, Navikas V, Mahecic D, Manley S, Radenovic A, Experimental combination of super-resolution optical fluctuation imaging with structured illumination microscopy for large fields-of-view, *ACS Photonics* **8**, 2440 (2021). https://doi.org/10.1021/acsphotonics.1c00668.

52 Tenne R, Rossman U, Rephael B, Israel Y, Krupinski-Ptaszek A, Lapkiewicz R, Silberberg Y, Oron D, Super-resolution enhancement by quantum image scanning microscopy, *Nat. Photonics* **13**, 116 (2019). https://doi.org/10.1038/s41566-018-0324-z.

53 Picariello F, Losero E, Tchernij SD, Boucher P, Genovese M, Ruo-Berchera I, Degiovanni IP, *Quantum super-resolution microscopy by photon statistics and structured light*, 2024. https://doi.org/10.48550/arXiv.2408.11654

54 https://en.wikipedia.org/wiki/RESOLFT.

55 Hell SW, Far-field optical nanoscopy, *Science* **316**, 1153 (2007). https://doi.org/10.1126/science.1137395.

56 Hanne J, Falk HJ, Görlitz F, Hoyer P, Engelhardt J, Sahl SJ, Hell SW, STED nanoscopy with fluorescent quantum dots, *Nat. Commun.* **6**, 7127 (2014). https://doi.org/10.1038/ncomms8127.

57 Han KY, Willig KI, Rittweger E, Jelezko F, Eggeling C, Hell SW, Three-dimensional stimulated emission depletion microscopy of nitrogen-vacancy centers in diamond using continuous-wave light, *Nano Lett.* **9**, 3323 (2009). https://doi.org/10.1021/nl901597v.

58 Hell SW, Toward fluorescence nanoscopy, *Nat. Biotechnol.* **21**, 1347 (2003). https://doi.org/10.1038/nbt895.

59 Schermelleh L, Heintzmann R, Leonhardt H, A guide to super-resolution fluorescence microscopy, *J. Cell Biol.* **190**, 165 (2010). https://doi.org/10.1083/jcb.201002018.

60 Rittweger E, Wildanger D, Hell SW, Far-field fluorescence nanoscopy of diamond color centers by ground state depletion, *Europhys. Lett.* **86**, 14001 (2009). https://doi.org/10.1209/0295-5075/86/14001.

61 Fujita K, Kobayashi M, Kawano S, Yamanaka M, Kawata S, High-resolution confocal microscopy by saturated excitation of fluorescence, *Phys. Rev. Lett.* **99**, 228105 (2007). https://doi.org/10.1103/PhysRevLett.99.228105.

62 Jagadale TC, Murali DS, Chu SW, Nonlinear absorption and scattering of a single plasmonic nanostructure characterized by X-scan technique, *Beilstein J. Nanotechnol.* **10**, 2182 (2019). https://doi.org/10.3762/bjnano.10.211.

63 Chu SW, Wu HY, Huang YT, Su TY, Lee H, Yonemaru Y, Yamanaka M, Oketani R, Kawata S, Shoji S, Fujita K, Saturation and reverse saturation of scattering in a single plasmonic nanoparticle, *ACS Photonics* **1**, 32 (2014). https://doi.org/10.1021/ph4000218.

64 Lee H, Li KY, Huang YT, Shen PT, Deka G, Oketani R, Yonemaru Y, Yamanaka M, Fujita K, Chu SW, Measurement of scattering nonlinearities from a single plasmonic nanoparticle, *J. Vis. Exp.* **107**, e53338 (2016). https://doi.org/10.3791/53338.

65 Kauranen M, Zayats AV, Nonlinear plasmonics, *Nat. Photonics* **6**, 737 (2012). https://doi.org/10.1038/nphoton.2012.244.

66 Wu HY, Huang YT, Shen PT, Lee H, Oketani R, Yonemaru Y, Yamanaka M, Shoji S, Lin KH, Chang CW, Kawata S, Ultrasmall all-optical plasmonic switch and its application to superresolution imaging, *Sci. Rep.* **6**, 24293 (2016). https://doi.org/10.1038/srep24293.

67 Hädrich M, Siefke T, Banasch M, Zeitner UD, Optical metasurfaces made by cell projection lithography: Electron beam nanopatterning with high optical quality on large areas, *PhotonicsViews* **19**, 28 (2022). https://doi.org/10.1002/phvs.202200036.

68 Mazaheri Z, Koral C, Andreone A, Marino A, Terahertz time-domain ellipsometry: tutorial, *J. Opt. Soc. Am. A* **39**, 1420 (2022). https://doi.org/10.1364/josaa.463969.

69 Rittweger E, Han KY, Irvine SE, Eggeling C, Hell SW STED microscopy reveals crystal colour centres with nanometric resolution, *Nat. Photonics* **3**, 144 (2009). https://doi.org/10.1038/nphoton.2009.2.

70 Balasubramanian G, Lazariev A, Arumugam SR, Duan DW, Nitrogen-vacancy color center in diamond-emerging nanoscale applications in bioimaging and biosensing, *Curr. Opin. Chem. Biol.* **20**, 69 (2014). https://doi.org/10.1016/j.cbpa.2014.04.014.

71 Aprà P, Amine NH, Britel A, Sturari S, Varzi V, Ziino M, Mino L, Olivero P, Picollo F, Creation, control, and modeling of NV centers in nanodiamonds, *Adv. Funct. Mater.* **34**, 2404831 (2014). https://doi.org/10.1002/adfm.202404831.

72 Aprà P, Ripoll-Sau J, Manzano-Santamaría J, Munuera C, Forneris J, Tchernij SD, Olivero P, Picollo F, Vittone E, Ynsa MD, Structural characterization of 8 MeV ^{11}B implanted diamond, *Diam. Relat. Mater.* **104**, 107770 (2020). https://doi.org/10.1016/j.diamond.2020.107770.

73 Wang M, Zhang C, Yan S, Chen T, Fang H, Yuan X, Wide-field super-resolved Raman imaging of carbon materials, *ACS Photonics* **8**, 1801 (2021). https://doi.org/10.1021/acsphotonics.1c00392.

74 Chen H, Wu X, Zhang Y, Yang Y, Min C, Zhu S, Yuan X, Bao Q, Bu J, Wide-field in situ multiplexed Raman imaging with superresolution, *Photonics Res.* **6**, 530 (2018). https://doi.org/10.1364/PRJ.6.000530.

75 Müller M, Mönkemöller V, Hennig S, Hübner W, Huser T, Open-source image reconstruction of super-resolution structured illumination microscopy data in ImageJ, *Nat. Commun.* **7**, 10980 (2016). https://doi.org/10.1038/ncomms10980.

76 Ditalia Tchernij S, Luhmann T, Herzig T, Kupper J, Damin A, Santonocito S, Signorile M, Traina P, Moreva E, Celegato F, Pezzagna S, Single-photon emitters in lead-implanted single-crystal diamond, *ACS Photonics* **5**, 4864 (2018). https://doi.org/10.1021/acsphotonics.8b01013.

77 Salditt T, Egner A, Luke DR, *Nanoscale photonic imaging* (Springer Nature, 2020).

78 Pinhas H, Wagner O, Danan Y, Danino M, Zalevsky Z, Sinvani M, Plasma dispersion effect based super-resolved imaging in silicon, *Opt. Express* **26**, 25370 (2018). https://doi.org/10.1364/OE.26.025370.

79 Tzang O, Pevzner A, Marvel RE, Haglund RF, Cheshnovsky O, Super-resolution in label-free photomodulated reflectivity, *Nano Lett.* **15**, 1362 (2015). https://doi.org/10.1021/nl504640e.

80 Bundesmann C, Neumann H, Tutorial: The systematics of ion beam sputtering for deposition of thin films with tailored properties, *J. Appl. Phys.* **124**, 231102 (2018). https://doi.org/10.1063/1.5054046.

81 Lazar J, Klapetek P, Valtr M, Hrabina J, Buchta Z, Cip O, Cizek M, Oulehla J, Sery M, Short-range six-axis interferometer controlled positioning for scanning probe microscopy, *Sensors* **14**, 877 (2014). https://doi.org/10.3390/s140100877.